

Switchable Giant Bulk Photocurrents and Photo-spin-currents in Monolayer PT-symmetric Anti-ferromagnet MnPSe_3

Liang Liu, Weikang Liu, Bin Cheng, Bin Cui, Jifan Hu*

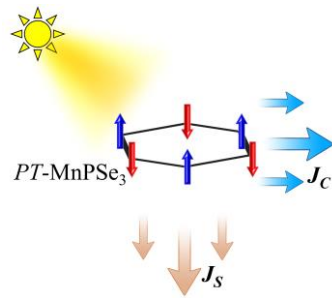
School of Physics, State key laboratory for crystal materials, Shandong University, Jinan 250100, China.

* To who should be corresponded: hujf@sdu.edu.cn

ABSTRACT

Converting light into steady currents and spin-currents in two-dimensional (2D) platform is essential for future energy harvesting and spintronics. We show that the giant and modifiable bulk photovoltaic effects (BPVEs) can be achieved in air-stable 2D antiferromagnet (AFM) monolayer MnPSe₃, with nonlinear photoconductance $> 4000 \text{ nm}\cdot\mu\text{A}/\text{V}^2$ and photo-spin-conductance $> 2000 \text{ (nm}\cdot\mu\text{A}/\text{V}^2 \cdot \hbar/2e)$ in the visible spectrum. The propagation and the spin-polarizations of photocurrents can be switched via simply rotating the Néel vector. We unveil that the PT -symmetry, mirror symmetries, and spin-orbital-couplings are the keys for the observed sizable and controllable 2D BPVEs. All the results provide insights into the BPVEs of 2D AFM, and suggest that the layered MnPSe₃ is an outstanding 2D platform for energy device and photo-spintronics.

TOC GRAPHIC



Anti-ferromagnetism enables efficient 2D solar cell in MnPSe₃ atomic thin layer.

Bulk photovoltaic effects (BPVEs) convert the incident light into steady currents in homogeneous crystals, sparking intense interests due to the potentials for energy harvesting, rectifications, spintronics, spectroscopes, etc.¹⁻⁹ BPVEs have been thought to be dominated by the profound shift mechanism,¹⁰⁻¹² in which the photocurrents are due to the continuous shifts of valence and conduction electrons in the non-centrosymmetric lattice during the photo-pumping processes. To date, the shift-type BPVEs have been realized in ferroelectrics,^{3, 8, 10, 13} piezoelectrics,¹⁴⁻¹⁷ and topological Weyl semimetals.¹⁸ On the other hand, it is also possible to generate BPVEs via injection mechanism in which the net photocurrents are due to the unbalances in group velocities amongst the photo-excited carriers.¹⁹⁻²⁰ Recently, several studies have predicted that the injection-type BPVEs can be observed in two-dimensional (2D) bilayer anti-ferromagnets (AFM) CrI₃⁷ and MnBi₂Te₄,^{9, 21} which possess the parity-temporal (*PT*) symmetry. *PT*-BPVEs are believed to be superior since the injection currents running in these systems are usually larger than the shift currents by several magnitude orders. More importantly, the incorporation of magnetism in BPVEs offers numerous modulation paths and opens a wealth of possibilities for opto-spintronic applications. However, the 2D materials suitable for *PT*-BPVE are very few in records. For the proposals of bilayer *PT*-AFM, the essential *PT*-symmetries stand on the long-range van der Waals (vdW) interlayer couplings,^{7, 9, 21-24} and the weak vdW strengths in these interactions limit the magnitudes of photocurrents. Besides, the ubiquitous layer-slides, twists in vdW bilayers²⁵ might break the *PT*-symmetries and harm the BPVEs. On the other hand, the poor magnetic and air stabilities of CrI₃ and MnBi₂Te₄ cannot fulfill the demanding of realistic applications perfectly.²¹⁻²⁴ Hence, it is quite desired to discovery better platforms to realize *PT*-BPVEs.

MnPSe₃ belongs to the family of transition metal thiophosphates (MPX₃, with M=Mn, Fe, Co, Ni; X=S, Se), which are layered magnetic semiconductors with band gaps suitable for visible light. And they are easy to be exfoliated to 2D layers with high qualities due to the ultra-weak vdW interlayer interactions and outstanding air stabilities.²⁶ So, they exhibit extraordinary performances in optoelectronic responses and opto-chemistry.²⁷⁻³² However, there are notable paucity of studies investigating the BPVEs in 2D MPX₃, since MPX₃ have centrosymmetric lattice and no shift-currents are allowed.³³⁻³⁵ Manganese thiophosphates are exceptional, the AFM hexagonal sublattice expanded by Mn²⁺ ions break the inversion symmetry (*P*-symmetry) and the *PT*-polarization is thus

hosted.³⁵⁻³⁶ Furthermore, the anti-ferromagnetism of MnPSe₃ is amenable to external modulations via strains and magnetic fields.³⁷ Therefore, it is intriguing to see if the *PT*-AFM MnPSe₃ can exhibit modulable and large *PT*-BPVEs.

In this work, we predict the *PT*-BPVEs of monolayer MnPSe₃ induced by the illuminations of linearly polarized visible light. Based on the first-principle calculations, we show that the *PT*-polarizations in MnPSe₃ are stabilized by the intra-layer AFM order and the strong spin-orbital-couplings (SOC). Surprisingly, the *PT*-polarizations can perfectly align the phases of local photocurrents in (P₂Se₆)⁴⁻ prisms, inducing large BPVEs with 2nd order photoconductance exceeding 4000 nm·μA/V² and photo-spin-conductance exceeding 2000 (nm·μA/V² ħ/2e) in the visible spectrum. We also unveil that the 2D BPVs and the Néel vectors are intimately intertwined through the mirror symmetries, enabling abundant controlling routes for photocurrents and photo-spin-currents. It is possible to regulate the magnitudes, switch the propagations, and reversing the spin polarizations of photocurrents via rotating the Néel vectors. Hence, MnPSe₃ is the ideal platform to realize 2D *PT*-BPVEs, providing opportunities for high-efficient energy and controllable opto-spintronic applications.

Figure 1(a) shows the lattice of MnPSe₃ that consists of (P₂Se₆)⁴⁻ prisms and two Mn-sublattices. Our density functional theory calculations indicate that the Mn²⁺ ions possess local magnetic moment of 5μB, and the nearest neighbored magnetic moments are anti-parallel, consist with previous studies.³⁶ The anti-ferromagnetic honeycomb framework of Mn-sublattices displayed in Fig. 1(a) breaks the *P*-symmetry because the *P*-operation interchanges the two Mn-sublattices with opposite magnetic moments. Once the *P*-operation is followed by time reversal (*T*) operation which reverses all the magnetic moments, the system coincides with itself, that is, the *PT*-symmetry is preserved in the monolayer MnPSe₃. The lacking of *P*-symmetry indicates the MnPSe₃ monolayer is a polar crystal. This kind of polarization is apparently not related to the non-centrosymmetric crystal geometry but the AFM emerged from the strong interactions between electrons, and we call this as *PT*-polarization.

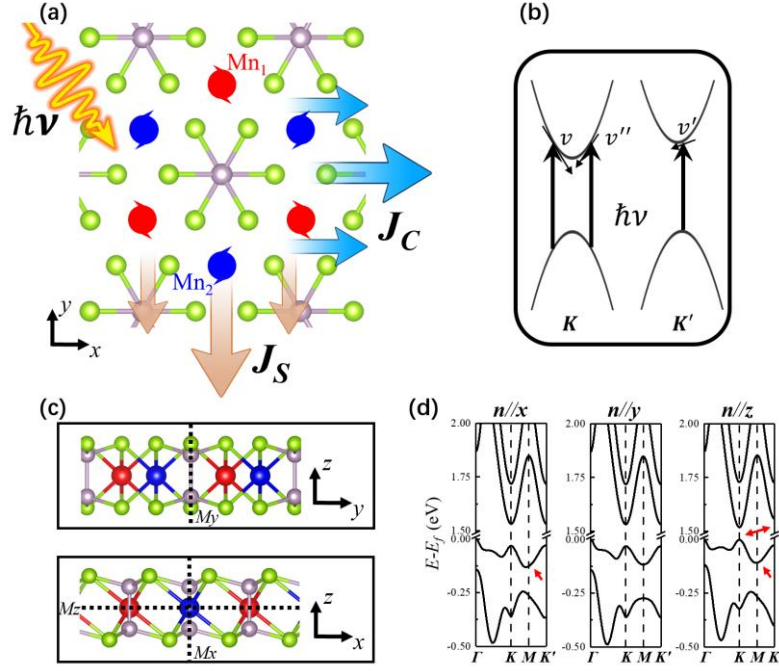


Figure 1. Lattice, magnetic, electronic, and photovoltaic structures of MnPSe₃. (a) The top view of monolayer MnPSe₃ lattice and the photocurrents and photo-spin-currents induced by the illuminations. The grey and green balls denote P and Se atoms. Blue and red balls denote the Mn atoms with opposite magnetic moments. (b) The typical dual valley structure in *PT*-AFM. Thick arrows denote the photo-induced hopping process and small arrows denote the group velocities of photo-excited holes. (c) The mirror reflections in MnPSe₃ monolayer. Dashed lines denote the mirror planes. (d) The band structure of MnPSe₃ with Néel vector orientation along *x*-, *y*-, and *z*-directions.

It is important to note that the *PT*-polarization found in this study is distinguished with previous reports on bilayer CrI₃⁷ and MnBi₂Te₄.^{9, 21} In those systems, the *PT*-polarizations depend on the stacking order of bilayers and the long-range interlayer AFM couplings across vdW gaps. On the contrary, the *PT*-polarization in MnPSe₃ is induced by the strong short-range intralayer AFM exchange couplings. In addition, the intralayer crystal structure, which is based on the sturdy covalence bonds, is also more stable than the interlayer structures, which are based on the long-range vdW interactions. As a result, the monolayer MnPSe₃ is expected to have more robust *PT*-polarization, larger nonlinear opto-electronic couplings, and better stability.

Figure 1(b) shows the basic process of injection-type BPVs enabled by the *PT*-polarization. *K*

and K' label the dual valleys with opposite momentum *i.e.*, $K' = -K$, and they are related to each other by P - and T -operation. Since both P - and T -symmetries are broken, the degenerations between K and K' valleys are no longer to be enforced by these two symmetries. On the other hand, the valley-polarizations are also ruled by the mirror symmetry since some mirror operations interchange the dual valleys. Given the fact that the mirror symmetries are readily switchable via simply rotating the Néel vectors, it is straight to see that the PT -AFM with suitable mirror symmetries possess controllable valley-polarizations, exhibiting intriguing electronic structures for modulable photoelectronic responses.

Figure 1(c) shows the two possible mirror operations in MnPSe_3 . The first one termed as M_y is the reflection about the mirror plane M_y which is vertical to the basal plane and crosses the (P_2Se_6) prisms. M_y interchanges the dual Mn-sublattices, and flips the magnetic moments with x/z -orientations. Therefore, MnPSe_3 with Néel vector along x/z -directions preserve the M_y -symmetry. The second mirror operation termed as M_xM_z is a combination of double reflections about the one mirror perpendicular and the other vertical to the atomic plane. The Mn-sublattices do not exchange under M_xM_z , and the magnetic moments along y -directions are also preserved in M_xM_z . So, for the MnPSe_3 with Néel vector along y -direction, the M_xM_z -symmetry is preserved. More essentially, since the M_xM_z -operation interchanges the dual valleys while M_y -operation does not, the valley-polarizations in MnPSe_3 are prohibited in M_xM_z -symmetric case but allowed in M_y -symmetric case. Therefore, via simply rotating the magnetization orientations, we can readily obtain desired mirror-symmetry and switch the valley-polarizations in MnPSe_3 .

Figure 1(d) shows the band structures of MnPSe_3 predicted by relativistic DFT, with Néel vectors along x -, y -, and z -directions. In all cases, the band gap emerged in the corners of Brillouin zone (BZ), either K or K' , indicating the valley structures dominate the low-energy opto-electronic responses. For the MnPSe_3 with magnetic moments along z -axis, the asymmetries between K and K' valleys are obvious. The energy gaps at K and K' are $\Delta_K = 1.5196$ eV and $\Delta_{K'} = 1.5838$ eV, corresponding to the valley-polarization energy of 64.2 meV, which is a large value and consistent with previous studies.³⁶ For the case with Néel vectors along x -axis, we have $\Delta_K = 1.5632$ eV and $\Delta_{K'} = 1.5635$ eV, so the valley-polarization energy shrinks to 0.3 meV. The reason for this significant shrinking is that the valley-polarization is proportional to the efficiency of spin-orbit-coupling

(SOC), and the system with magnetizations along x -axis exhibits negligible SOC for BZ corner states. In 2D systems, the orbital moments of Bloch electrons around the BZ corners are dominated by the z -component, the z -orientated spins thus display the strongest SOC and valley-polarizations. For the y -magnetization, the valley polarization is forbidden by $M_x M_y$ -symmetry and $\Delta_K = \Delta_{K'} = 1.5634$ eV.

Besides, the symmetric aspects of band structure on the inner part of BZ also show clear dependences on the magnetization orientation. For MnPSe₃ with Néel vectors along x - and z -directions, the asymmetries of valence bands about M point are shown by the red arrows marked in Fig. 1(d). The extents of band asymmetries are similar in x - and z -magnetized cases, indicating that the orbital moments around M point have comparable x - and z -components, so that the efficiencies of SOC in these states are close to each other.

BPVE is the 2nd order opto-electronic responses, and the photocurrents j_C^μ can be phenomenologically expressed as: $j_C^\mu = \text{Re} \sum_{\alpha\beta} \sigma_C^{\mu:\alpha\beta}(0; \omega, -\omega) E^\alpha(\omega) E^\beta(-\omega)$, where μ , α , and β can be $x/y/z$ directions. ω denotes the frequency of photons. $\sigma_C^{\mu:\alpha\beta}$ is the 3-ranked tensor of BPVE photoconductance, $E^{\alpha\beta}$ denotes the α/β component of electric fields of incident light. For the system with P -symmetry, the P -operation will reverse the j_C^μ in l.h.s. but preserve the r.h.s., leading to the vanishing of BPVEs. So, the anti-ferromagnetism which produces PT -polarizations and lifts the P -symmetry in MnPSe₃ is the key for the nonzero BPVEs. On the other hand, although $\sigma_C^{\mu:\alpha\beta}$ always breaks the T -symmetry due to the relaxation dynamics of photo-induced carriers which lacks time reciprocities, the details of how the T -symmetry is broke decides the magnitude and direction of PT -polarization, thus is also significantly relevant to PT -BPVEs.¹⁹

In the following, we focus on the BPVEs generated by the light which are linearly polarized in x -axis, and only the real part of $\sigma_C^{x:xx}$ and $\sigma_C^{y:xx}$ are relevant. Other directions of BPVE can be obtained by the considerations on symmetry. Microscopically, the BPVE can be evaluated by the nonlinear response theory, and the dominated contribution is expressed as: ^{7, 20, 38}

$$\sigma_C^{\mu:\alpha\beta}(0; \omega, -\omega) = \frac{2e^3}{S\omega^2} \sum_{k \in \text{BZ}} \sum_{lmn, \Omega = \pm\omega} f_{ln} \frac{v_{k,mn}^\mu v_{k,nl}^\alpha v_{k,lm}^\beta}{(E_{k,mn} - i\hbar/\tau)(E_{k,lm} - \hbar\Omega)} \quad (1)$$

here k labels the k -point in irreducible BZ and l, m, n label the band index, $v_{k,lm}^\mu$ is the matrix

elements of velocity operator, $E_{k,ml} = E_{k,m} - E_{k,l}$ denotes the difference in band energies, $f_{ln} = f_l - f_n$ is the difference of occupations in l^{th} and n^{th} bands. ω is the magnitude of frequency of incident light. τ is the relaxation time for intra-band process. In principle, the relaxation time τ might depend on momentum, band indices, and frequencies of light, because of impurity scattering, electron-phonons couplings, many-body interactions, etc. However, several previous studies have showed that it is still reasonable to consider an average and constant relaxation time approximation in the calculations of BPVEs.³⁹⁻⁴⁰ Hence, in this study we adopt the constant relaxation time approximation and take the default value $\hbar/\tau = 1 \text{ meV}$, i.e., $\tau \approx 0.6 \text{ ps}$ by default. This setting is rather conservative since the MnPSe₃ is supposed to be a clean crystal due to its excellent chemical stabilities. S is the area of MnPSe₃ cell. Since the thickness of 2D monolayer is not well-defined, we do not average the photoconductance over volume but area. So, the σ_C calculated in eq. 1 is related to conventional definition of 2nd order photoconductances in 3D systems σ_C^{3D} by $\sigma_C = L\sigma_C^{3D}$, in which L is the effective thickness of 2D monolayer. And the unit of σ_C in eq. 1 is $\text{nm} \cdot \mu\text{A}/\text{V}^2$.

Figure 2 shows the calculated nonlinear photoconductance of BPVE. For MnPSe₃ with Néel vector along z -axis [Fig. 2(a)], $\sigma_C^{x:xx}$ exhibits several peaks in the visible spectrum with photon energy range from 1.6 eV to 3.6 eV. The first peak of $\sigma_C^{x:xx}$ occurs at 1.83 eV, slighter higher than the energy gap of $\sim 1.5 \text{ eV}$. The peak value is $-187 \text{ (nm} \cdot \mu\text{A}/\text{V}^2)$, which is comparable to the highest BPVE conductance previously reported in bilayer AFM systems.^{7,9} The strongest peak of $\sigma_C^{x:xx}$ is at 2.98 eV, with magnitude $4152 \text{ (nm} \cdot \mu\text{A}/\text{V}^2)$, which is ~ 10 -folds larger than the previous proposals. On the other hand, $\sigma_C^{y:xx}$ vanishes at all photon energies, consistent with the M_y -symmetry since $\sigma_C^{y:xx}$ is proportional to $v_y \times v_x \times v_x$ which is odd in M_y -reflection. Therefore, the photocurrents induced by the linearly polarized light only propagate along the x -axis in this case.

Note that because of the injection mechanism of BPVEs in MnPSe₃, the magnitude of photoconductance is proportional to the value of relaxation time.^{7, 20} The explicit dependence of BPVEs on relaxation time are shown in Fig. S1 in supporting information. Since the utilized relaxation time constants of 0.6ps is conservative, the estimations on the BPVEs should be conservative, too.

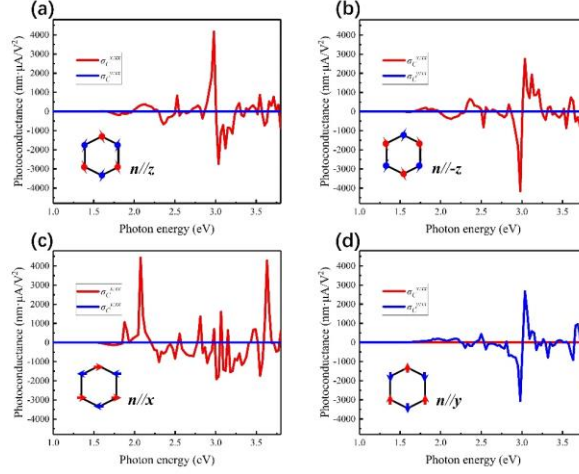


Figure 2. Photoconductance $\sigma_c^{x:xx}$ and $\sigma_c^{y:xx}$ for MnPSe₃ with Néel vector along (a) z -direction, (b) $-z$ -direction, (c) x -direction, and (d) y -direction. The hexagon in the left-down part of each figure denotes the magnetic lattice formed by Mn²⁺ ions, and the arrows on it denote the orientations of local magnetic moments. The directions of Néel vectors are marked aside the hexagons.

Then we reverse the Néel vector to $-z$ -direction, and the $\sigma_c^{x:xx}$ displayed in Fig. 2(b) becomes the opposite of the case discussed before, indicating that the propagation directions of photocurrents are locked with the orientation of Néel vectors. This is in consistency with our previous discussions on T -symmetry i.e., the photocurrent propagation is related to PT -polarization, which is further controlled by the magnetizations. And this behavior suggests a promising route to read out the nonvolatile information stored as Néel vectors in MnPSe₃ via the BPVEs, which is essential for the 2D opto-spintronic memories.

Fig. 2(c) displays the photoconductance of MnPSe₃ with Néel vector along x -axis. Once again, due to the M_y -symmetry, $\sigma_c^{y:xx}$ is zero everywhere. The first peak of $\sigma_c^{x:xx}$ now occurs around 1.73 eV with value -100 (nm $\cdot\mu$ A/V²), and the highest peak of $\sigma_c^{x:xx}$ in Fig. 1(c) is 4436 (nm $\cdot\mu$ A/V²) at 2.02 eV. Comparing to the $\pm z$ -cases discussed before, the photocurrents induced by low-energy photons is smaller here. This can be explained by the valley structures show in Fig. 1(d). Since the valley-polarizations in x -magnetized system are much smaller, the low-energy photoconductance, which is dominated by the valley-polarization, should be weaker. Besides, the several high peaks in Fig. 2(c) have magnitudes comparable with $\pm z$ -magnetized cases, revealing that the high-energy

photoconductance is free from the valley-related opto-electronic processes.

Fig. 2(d) displays the case with Néel vector along y -axis. $\sigma_C^{x:xx}$ becomes zero at all photon energies, thus the photocurrents generated by linearly polarized light run in y -axis solely. This perpendicular switching of photocurrents propagation is caused by the switching of mirror symmetries from M_y to M_xM_z , which is brought about by the rotations of Néel vectors from x/z -axis to y -axis. The $\sigma_C^{x:xx}$ is odd in M_y mirror operation, thus no photocurrents in x -axis are allowed. For $\sigma_C^{y:xx}$, it reaches the first peak at 1.97 eV with value 241 ($\text{nm}\cdot\mu\text{A}/\text{V}^2$), and the highest peak value is -3059 ($\text{nm}\cdot\mu\text{A}/\text{V}^2$) occurred at photon energy of 2.98 eV.

In addition, the 2D BPVEs of MnPSe_3 also generate pure spin-currents. We detect the spin-resolved photocurrents with vector potentials projected to spin tunnels, and compute the nonlinear photo-spin-conductance tensor $\sigma_{S_z}^{\mu:\alpha\beta}$, which is relevant for spin-currents (See supporting information for more details). The spin polarizations in photocurrents are dominated by the z -component in most cases, we thus focused on the photo-spin-conductance with z -polarization, which are displayed in Figure 3.

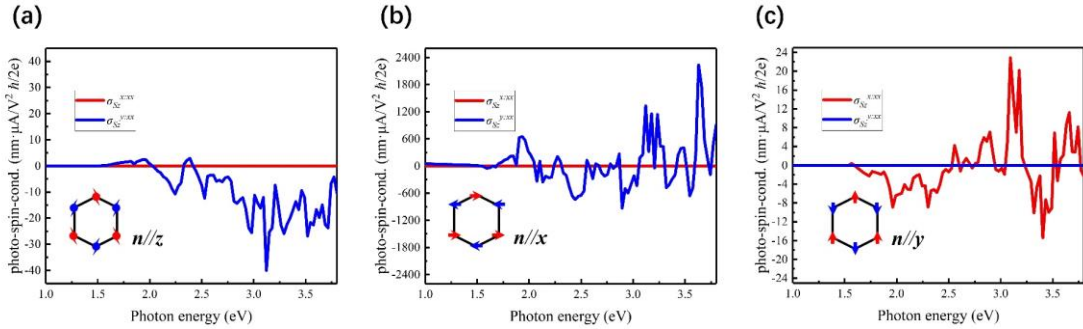


Figure 3. Photo-spin-conductance $\sigma_{S_z}^{x:xx}$ and $\sigma_{S_z}^{y:xx}$ for MnPSe_3 with Néel vector along (a) z -direction, (b) x -direction, and (c) y -direction.

Figure 3(a) shows the photo-spin-conductance in system with Néel vectors along z -axis. Firstly, $\sigma_{S_z}^{x:xx}$ vanishes at all energies. $\sigma_{S_z}^{y:xx}$ acquires its first peak value 6 ($\text{nm}\cdot\mu\text{A}/\text{V}^2 \hbar/2e$) around 1.99 eV. The highest peak value is -40 ($\text{nm}\cdot\mu\text{A}/\text{V}^2 \hbar/2e$) occurred at photon energy of 3.12 eV. When the Néel vector rotate to x -axis, $\sigma_{S_z}^{x:xx}$ keeps zero values, but the $\sigma_{S_z}^{y:xx}$ is drastically enlarged [Fig. 3(b)]. The first peak of $\sigma_{S_z}^{y:xx}$ is -48 ($\text{nm}\cdot\mu\text{A}/\text{V}^2 \hbar/2e$) at 1.61 eV. The strongest $\sigma_{S_z}^{y:xx}$ peak in Fig. 3(b) is

2237 ($\text{nm}\cdot\mu\text{A}/\text{V}^2 \hbar/2e$) at 3.6 eV. For the MnPSe_3 with Néel vector in y -axis, $\sigma_{S_z}^{x:xx}$ presents finite magnitudes while $\sigma_{S_z}^{y:xx}$ vanishes [Fig. 3(c)]. And $\sigma_{S_z}^{x:xx}$ get the first peak at 1.75 eV with value -2 ($\text{nm}\cdot\mu\text{A}/\text{V}^2 \hbar/2e$), and the largest $\sigma_{S_z}^{x:xx}$ takes place at 3.09 eV with value 23 ($\text{nm}\cdot\mu\text{A}/\text{V}^2 \hbar/2e$).

Hence, the photo-spin-currents are modulable via rotating the Néel vectors, which can be explained by the switching of mirror symmetries. The photo-spin-conductance is related to the conventional photoconductance by the equation $\sigma_{S_z} = s_z \times \sigma_C$, and s_z is odd about both M_y - and $M_x M_z$ -reflections. Therefore, the allowed propagation directions of spin currents (with s_z -polarization) are always orthogonal to the charge currents, i.e., the spin currents found here are pure without the net movements of charges, which are desired for the low-consumption spintronics. Besides, it worths noticing that the photo-spin-conductance for cases with Néel vectors along x -axis is stronger than the other two cases by magnitude orders, indicating that the photon-to-spin conversions is switched from shift-dominated mechanism to injection-dominated mechanism along with the rotations of Néel vectors from y/z - to x -axis. This change in mechanism is further supported by the analysis of the dependence of photo-spin-conductance on relaxation time (see Fig. S2 in supporting information for more details). The injection-type spin-currents are intriguing and distinguished from the previous reports,⁴¹⁻⁴² and the significantly large injection-spin-currents might open a new way for robust spin-currents generations via illuminations.

To further investigate the structure of BPVs in MnPSe_3 , we plot the Brillouin zone (BZ) distribution of photoconductance in Figure 4. The photon energy is 2.98 eV, corresponding to the position of the strongest BPVE in Fig. 2. The most relevant states to the BPVE form several butterfly-like regions in BZ. and their contributions and positions are controlled by the orientations of Néel vectors, leading to the modulations on BPVE. Fig. 4(a) displays the BZ-distributions of $\sigma_C^{x:xx}$. The states in right part of BZ have positive crystal moments in x -direction and positively contribute to the $\sigma_C^{x:xx}$ (blue colored), while the states in left part of BZ are negatively related to the net $\sigma_C^{x:xx}$ (red colored). The topmost inset in Fig. 4(a) shows the case with Néel vectors along $+z$ -direction. The most relevant states are located at the right part of BZ. The contributions from individual Bloch states reach as high as 4×10^6 ($\text{nm}\cdot\mu\text{A}/\text{V}^2$), three orders larger than the net value of $\sigma_C^{x:xx}$, indicating the net BPVE is the residual effect of many counteracting contributions. It is thus hopeful to obtain ultra-large BPVE if one can optically excite the states with specific crystal

momentums. When Néel vectors rotate to $+x$ -direction [top right in Fig. 4(a)], the contributions from left and right parts of BZ are both clear. For Néel vectors in $+y$ -direction [bottom right in Fig. 4(a)], the contribution regions move to the up part of BZ and become anti-symmetric to each other, in line with the zero-value of $\sigma_C^{x:xx}$ in this case. The lowest inset in Fig. 4(a) shows the case with Néel vectors in $-z$ -direction. The contributions are dominated by the left part of BZ with negative values, which is exactly the opposite of the case displayed in the topmost inset. Further rotating the Néel vectors to $-x$ - and $-y$ -directions, we see the BZ-distributions of BPVE contributions are the opposite of $+x$ - and $+y$ -cases.

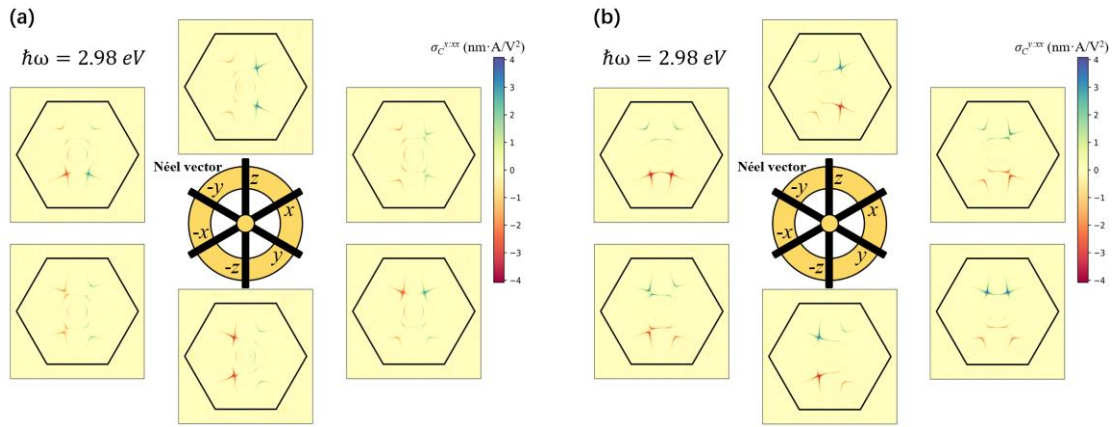


Figure 4. Photoconductances distributions on Brillouin zone that depend on the direction of Néel vector of MnPSe₃. (a) The BZ distributions of $\sigma_C^{x:xx}$. (b) The BZ distributions of $\sigma_C^{y:xx}$. The incident light is linearly polarized in x -axis, with photon energy of 2.98 eV. The distributions placed at top, top right, bottom right, bottom, bottom left, and up left correspond to the cases with Néel vectors along $+z$, $+x$, $+y$, $-z$, $-x$, and $-y$ directions. The hexagons are the irreducible Brillouin zone. For better illustrations, τ is set to 0.1 ps here.

Figure 4(b) displays the BZ-distributions of $\sigma_C^{y:xx}$. They have the same positions as the distributions of $\sigma_C^{x:xx}$ shown in Fig. 4(a), but the signs of contributions are different. The upper part of BZ corresponds to the Bloch states with positive crystal moments in y -direction, and the contributions in this region are blue, positively contributing to the net $\sigma_C^{y:xx}$. The contributions of lower part of BZ are in red color, exhibiting negative contributions to net $\sigma_C^{y:xx}$. For cases with Néel vectors along $\pm z$ - and $\pm x$ -directions, the contributions are anti-symmetric in the BZ, leading to the

zero BPVEs. Only if the Néel vectors orient to $\pm y$ -directions, the contributions from upper and lower parts of BZ are not anti-symmetric and nonzero BPVEs are permitted. All these results are in line with former discussions on symmetries and agree with the integrated results displayed in Fig. 2.

To further understand the PT -BPVE in local coordinates and figure out how the PT -polarizations interact with the dynamics of photo-electrons, we detect the real-space resolved photoconductance with vector potentials projected to hopping tunnels (See supporting information for more details), which are the spaces between atoms as shown in Fig. 5(a). Below, we focused on the cases with Néel vectors along z -axis.

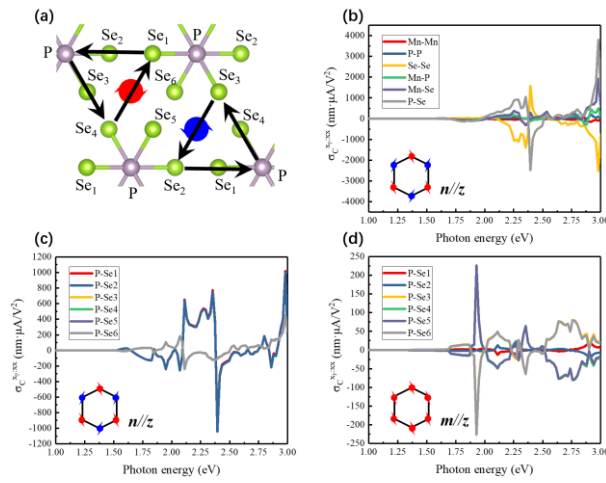


Figure 5. Bulk photoconductance projected to real-space. (a) Atomic positions and possible hopping tunnels in MnPSe_3 . The arrows denote several typical hopping tunnels in $(\text{P}_2\text{Se}_6)^{4-}$. (b) $\sigma_C^{x:xx}$ in AFM MnPSe_3 projected to six types of tunnels. (c) $\sigma_C^{x:xx}$ in AFM MnPSe_3 projected to six types of P-Se tunnels. (d) $\sigma_C^{x:xx}$ in FM MnPSe_3 projected to six types of P-Se tunnels.

We firstly classify the photoconductance $\sigma_C^{x:xx}$ into six types according to the hopping tunnels including Mn-Mn, P-P, Se-Se, Mn-P, Mn-Se, and P-Se. The photocurrents are emitted by the electron-hole combinations happened in either one of these tunnels. And the summation of all these six types is exactly equal to the net BPVE displayed in Fig. 2(a).

Figure 5(b) shows the contributions from the six types. Comparing to the total $\sigma_C^{x:xx}$ shown in Fig. 2(a), it is clear that the P-Se tunnels always dominate the BPVEs with highest value of 3795 ($\text{nm}\cdot\mu\text{A}/\text{V}^2$), while the contributions of Se-Se tunnels are comparable but they are negative and the strongest value is -2323 ($\text{nm}\cdot\mu\text{A}/\text{V}^2$). The Mn-Se tunnels are the third largest contributors, and its

highest peak is 1772 ($\text{nm}\cdot\mu\text{A}/\text{V}^2$). Other tunnels contribute negligibly to the BPVEs. Therefore, the BPVEs in MnPSe_3 are mainly emitted by the hopping processes in the sublattice expanded by $(\text{P}_2\text{Se}_6)^{4-}$ prisms.

Fig. 5(c) shows the $\sigma_C^{x:xx}$ further projected to the six types of P-Se tunnels, including tunnels of P-Se₁, P-Se₂, P-Se₃, P-Se₄, P-Se₅, P-Se₆. The summation of all these six P-Se types is identical to the contributions of P-Se tunnels displayed in Fig. 5(b) with grey lines. The real-space orientations of tunnels of P-Se₁ and P-Se₂ are close to the x -axis [See Fig. 5(a)], and their contributions are nearly coincided, showing the ideal phase alignment for the optoelectrical processes in these two tunnels. And they constitute the most parts of photocurrents in the $(\text{P}_2\text{Se}_6)^{4-}$ prism sublattice with highest peak values of ~ 1000 ($\text{nm}\cdot\mu\text{A}/\text{V}^2$). This ideal phase alignment is surprising since these two tunnels are not symmetric counterparts in AFM MnPSe_3 . The contributions from the other four P-Se tunnels are moderate, and their strongest peak value is 441 ($\text{nm}\cdot\mu\text{A}/\text{V}^2$). They coincide with each other due to the M_y -mirror symmetry.

Fig. 5(d) shows the $\sigma_C^{x:xx}$ projected to the six P-Se tunnels [as the case in Fig. 5(c)] for the MnPSe_3 with parallel magnetic moments along z -axis, that is, the ferromagnetic (FM) case. Although the P symmetry of FM MnPSe_3 enforces the zero value for total BPVEs, the local contributions are generally nonzero. The contributions from P-Se₁ and P-Se₂ tunnels are heavily suppressed in this case, and the highest peak value is only 21 ($\text{nm}\cdot\mu\text{A}/\text{V}^2$), 100 times smaller than the AFM case displayed in Fig. 5(c). On the other hand, the contributions of the other four P-Se tunnels show peak values of 227 ($\text{nm}\cdot\mu\text{A}/\text{V}^2$), which is comparable to the AFM case, especially in the low phonon energy range (< 2 eV). Therefore, on the view of local photoelectrical responses, the role of AFM order in Mn-sublattices is two-folds: aligning the phases of photocurrents, and enhancing the photon-to-currents efficiencies in the direction of PT -polarization (x -direction in present case).

In summary, we found the 2D monolayer MnPSe_3 is promising to realize large and controllable PT -BPVEs. The 2nd order photoconductance and photo-spin-conductance exceed 4000 ($\text{nm}\cdot\mu\text{A}/\text{V}^2$) and 2000 ($\text{nm}\cdot\mu\text{A}/\text{V}^2 \hbar/2e$) in the visible spectrum. Both the propagations and the spin-polarizations of photocurrents are switchable via rotating the Néel vectors. These switching are enabled by the mirror symmetries, which depend on the magnetization. The intralayer AFM orders of Mn^{2+}

sublattice show essential roles in the 2D BPVEs, since they can stabilize the PT -polarizations and lead to the phase alignments of photocurrents in the sublattice of $(P_2Se_6)^+$. Furthermore, we showed that the PT -BPVEs in $MnPSe_3$ are dominated by a small part of Bloch states in BZ, whose positions and contributions are intimately controlled by the Néel vectors. All these results shed light into the PT -BPVEs in 2D anti-ferromagnets, and indicate that the 2D monolayer $MnPSe_3$ is an ideal platform to achieve extraordinary PT -BPVEs, meriting future energy and spintronic applications.

Computational Method. The geometry optimization and electronic structure of $MnPSe_3$ in ground state are calculated within Vienna atomic simulation pack (VASP),⁴³ based on relativistic density functional theory (DFT). Projected augmentation plane wave basis (PAW) is utilized and the plane waves are cutoff at 400 eV. The exchange-correlation effects amongst electrons are captured via generalized gradient approximation (GGA) with the functional of Perdew-Burke-Ernzerh (PBE) form.⁴⁴ A vacuum layer of 20 Å is set to isolate the layers in nonperiodic direction to eliminate the unphysical interactions between neighboring slabs. Brillouin zone is sampled with a Γ -centered k -mesh $10 \times 10 \times 1$ using Monkhorst-Pack scheme.⁴⁵ The geometry relaxation is carried out until the maximum force is smaller than 0.001 eV/Å. Energy convergent criteria for the self-consistent iterative calculations on the electronic structures is 10^{-6} eV/atom.

Since the GGA functional usually underestimates the strong interactions between d-electrons of transition metal compounds (in our case, standard GGA leads to metal ground states of $MnPSe_3$, which is inconsistent with the experiments), we employed the GGA + U_{eff} method with $U_{\text{eff}} = 3.0$ eV for d-electrons of Mn. This value of U_{eff} leads to the correct magnetic ground states and is in line with former studies on the $MnPSe_3$.³²

For the calculations of BPVE based on eq. 1 and related expressions, we construct the effective real-space tight-binding Hamiltonian via projecting the Bloch states obtained from relativistic DFT into the Hilbert space expanded by Wannier orbitals using WANNIER90,⁴⁶⁻⁴⁷ then the k -space Hamiltonians on general k -points are interpolated by solving the eigen-equations. The Wannier orbital basis include the 3d and 4s orbitals for Mn ions, 3s and 3p orbitals for P ions, and 4s and 4p orbitals for Se ions. It is found that the effective tight-binding Hamiltonian can reproduce the

electronic states predicted by relativistic DFT and the band structures of the effective model and the DFT coincide everywhere in the relevant energy window (see Figure S3 in Supporting information for more details), revealing the efficiency of the basis transformation. The k-grid utilized for the Brillouin zone integration in equation 1 is $800 \times 800 \times 1$. A denser k-grid $1600 \times 1600 \times 1$ is used to test the convergence of k-mesh sampling and we find the difference $< 5\%$.

Notes

The authors declare no competing financial interest.

ACKNOWLEDGMENT

This work was supported by Natural Science Foundation of Shandong (Grant No. ZR2022QA019), National Natural Science Foundation of China (Grant Nos. 12074221, 52171181, 52002222, 51472150, 2021-869, 11904204).

Supporting information available: Extracting out the expression of BPVEs from potentials; Expressions of spin and real-space projected BPVEs.

REFERENCES

- (1) Kraut, W.; von Baltz, R. Anomalous Bulk Photovoltaic Effect in Ferroelectrics: A Quadratic Response Theory. *Physical Review B* **1979**, *19*, 1548-1554.
- (2) von Baltz, R.; Kraut, W. Theory of the Bulk Photovoltaic Effect in Pure Crystals. *Physical Review B* **1981**, *23*, 5590-5596.
- (3) Choi, T.; Lee, S.; Choi, Y. J.; Kiryukhin, V.; Cheong, S.-W. Switchable Ferroelectric Diode and Photovoltaic Effect in BiFeO_3 . *Science* **2009**, *324*, 63-66.
- (4) Yang, S. Y.; Seidel, J.; Byrnes, S. J.; Shafer, P.; Yang, C. H.; Rossell, M. D.; Yu, P.; Chu, Y. H.; Scott, J. F.; Ager, J. W., 3rd, et al. Above-Bandgap Voltages from Ferroelectric Photovoltaic Devices. *Nature nanotechnology* **2010**, *5*, 143-147.
- (5) Daranciang, D.; Highland, M. J.; Wen, H.; Young, S. M.; Brandt, N. C.; Hwang, H. Y.; Vattilana, M.; Nicoul, M.; Quirin, F.; Goodfellow, J., et al. Ultrafast Photovoltaic Response in Ferroelectric Nanolayers. *Phys Rev Lett* **2012**, *108*, 087601.
- (6) Spanier, J. E.; Fridkin, V. M.; Rappe, A. M.; Akbashev, A. R.; Polemi, A.; Qi, Y.; Gu, Z.; Young, S. M.; Hawley, C. J.; Imbrenda, D. Power Conversion Efficiency Exceeding the Shockley–Queisser Limit in a Ferroelectric Insulator. *Nature Photonics* **2016**, *10*, 611-616.
- (7) Zhang, Y.; Holder, T.; Ishizuka, H.; de Juan, F.; Nagaosa, N.; Felser, C.; Yan, B. Switchable Magnetic Bulk Photovoltaic Effect in the Two-Dimensional Magnet CrI_3 . *Nature Communication* **2019**, *10*, 3783.

- (8) Li, Y.; Fu, J.; Mao, X.; Chen, C.; Liu, H.; Gong, M.; Zeng, H. Enhanced Bulk Photovoltaic Effect in Two-Dimensional Ferroelectric CuInP₂S₆. *Nature Communication* **2021**, *12*, 5896.
- (9) Xu, H.; Wang, H.; Zhou, J.; Li, J. Pure Spin Photocurrent in Non-Centrosymmetric Crystals: Bulk Spin Photovoltaic Effect. *Nature Communication* **2021**, *12*, 4330.
- (10) Paillard, C.; Bai, X.; Infante, I. C.; Guennou, M.; Geneste, G.; Alexe, M.; Kreisel, J.; Dkhil, B. Photovoltaics with Ferroelectrics: Current Status and Beyond. *Adv Mater* **2016**, *28*, 5153-5168.
- (11) Sipe, J. E.; Shkrebti, A. I. Second-Order Optical Response in Semiconductors. *Physical Review B* **2000**, *61*, 5337.
- (12) Fridkin, V. M. Bulk Photovoltaic Effect in Noncentrosymmetric Crystals. *Crystallography Reports* **2001**, *46*, 654-658.
- (13) Lee, D.; Baek, S. H.; Kim, T. H.; Yoon, J. G.; Folkman, C. M.; Eom, C. B.; Noh, T. W. Polarity Control of Carrier Injection at Ferroelectric/Metal Interfaces for Electrically Switchable Diode and Photovoltaic Effects. *Physical Review B* **2011**, *84*.
- (14) Yang, M.-M.; Kim Dong, J.; Alexe, M. Flexo-Photovoltaic Effect. *Science* **2018**, *360*, 904-907.
- (15) Mu, X.; Pan, Y.; Zhou, J. Pure Bulk Orbital and Spin Photocurrent in Two-Dimensional Ferroelectric Materials. *npj Computational Materials* **2021**, *7*.
- (16) Xu, H.; Wang, H.; Zhou, J.; Guo, Y.; Kong, J.; Li, J. Colossal Switchable Photocurrents in Topological Janus Transition Metal Dichalcogenides. *npj Computational Materials* **2021**, *7*.
- (17) Guo, Y.; Zhou, J.; Xie, H.; Chen, Y.; Wang, Q. Screening Transition Metal-Based Polar Pentagonal Monolayers with Large Piezoelectricity and Shift Current. *npj Computational Materials* **2022**, *8*.
- (18) Wang, Q.; Zheng, J.; He, Y.; Cao, J.; Liu, X.; Wang, M.; Ma, J.; Lai, J.; Lu, H.; Jia, S., et al. Robust Edge Photocurrent Response on Layered Type II Weyl Semimetal WTe₂. *Nature Communication* **2019**, *10*, 5736.
- (19) Holder, T.; Kaplan, D.; Yan, B. Consequences of Time-Reversal-Symmetry Breaking in the Light-Matter Interaction: Berry Curvature, Quantum Metric, and Adiabatic Motion. *Physical Review Research* **2020**, *2*.
- (20) Watanabe, H.; Yanase, Y. Chiral Photocurrent in Parity-Violating Magnet and Enhanced Response in Topological Antiferromagnet. *Physical Review X* **2021**, *11*.
- (21) Wang, H.; Qian, X. Electrically and Magnetically Switchable Nonlinear Photocurrent in P_T-Symmetric Magnetic Topological Quantum Materials. *npj Computational Materials* **2020**, *6*.
- (22) Huang, B.; Clark, G.; Navarro-Moratalla, E.; Klein, D. R.; Cheng, R.; Seyler, K. L.; Zhong, D.; Schmidgall, E.; McGuire, M. A.; Cobden, D. H., et al. Layer-Dependent Ferromagnetism in a Van Der Waals Crystal Down to the Monolayer Limit. *Nature* **2017**, *546*, 270-273.
- (23) Gong, Y.; Guo, J.; Li, J.; Zhu, K.; Liao, M.; Liu, X.; Zhang, Q.; Gu, L.; Tang, L.; Feng, X., et al. Experimental Realization of an Intrinsic Magnetic Topological Insulator. *Chinese Physics Letters* **2019**, *36*.

- (24) Otrokov, M. M.; Klimovskikh, II; Bentmann, H.; Estyunin, D.; Zeugner, A.; Aliev, Z. S.; Gass, S.; Wolter, A. U. B.; Koroleva, A. V.; Shikin, A. M., et al. Prediction and Observation of an Antiferromagnetic Topological Insulator. *Nature* **2019**, *576*, 416-422.
- (25) Cao, Y.; Fatemi, V.; Fang, S.; Watanabe, K.; Taniguchi, T.; Kaxiras, E.; Jarillo-Herrero, P. Unconventional Superconductivity in Magic-Angle Graphene Superlattices. *Nature* **2018**, *556*, 43-50.
- (26) Susner, M. A.; Chyasnavichyus, M.; McGuire, M. A.; Ganesh, P.; Maksymovych, P. Metal Thio- and Selenophosphates as Multifunctional Van Der Waals Layered Materials. *Adv Mater* **2017**, *29*.
- (27) Huang, H.; Shang, M.; Zou, Y.; Song, W.; Zhang, Y. Iron Phosphorus Trichalcogenide Ultrathin Nanosheets: Enhanced Photoelectrochemical Activity under Visible-Light Irradiation. *Nanoscale* **2019**, *11*, 21188-21195.
- (28) Lee, J.-U.; Lee, S.; Ryoo, J. H.; Kang, S.; Kim, T. Y.; Kim, P.; Park, C.-H.; Park, J.-G.; Cheong, H. Ising-Type Magnetic Ordering in Atomically Thin FeP₃. *Nano Letters* **2016**, *16*, 7433-7438.
- (29) Ramos, M.; Carrascoso, F.; Frisenda, R.; Gant, P.; Mañas-Valero, S.; Esteras, D. L.; Baldoví, J. J.; Coronado, E.; Castellanos-Gomez, A.; Calvo, M. R. Ultra-Broad Spectral Photo-Response in FeP₃ Air-Stable Devices. *npj 2D Materials and Applications* **2021**, *5*.
- (30) Zhu, W.; Gan, W.; Muhammad, Z.; Wang, C.; Wu, C.; Liu, H.; Liu, D.; Zhang, K.; He, Q.; Jiang, H., et al. Exfoliation of Ultrathin FeP₃ Layers as a Promising Electrocatalyst for the Oxygen Evolution Reaction. *Chem Commun (Camb)* **2018**, *54*, 4481-4484.
- (31) Kumar, R.; Jenjeti, R. N.; Austeria, M. P.; Sampath, S. Bulk and Few-Layer MnP₃: A New Candidate for Field Effect Transistors and Uv Photodetectors. *Journal of Materials Chemistry C* **2019**, *7*, 324-329.
- (32) Long, G.; Henck, H.; Gibertini, M.; Dumcenco, D.; Wang, Z.; Taniguchi, T.; Watanabe, K.; Giannini, E.; Morpurgo, A. F. Persistence of Magnetism in Atomically Thin MnP₃ Crystals. *Nano Lett* **2020**, *20*, 2452-2459.
- (33) Wildes, A. R.; Simonet, V.; Ressouche, E.; McIntyre, G. J.; Avdeev, M.; Suard, E.; Kimber, S. A. J.; Lançon, D.; Pepe, G.; Moubaraki, B., et al. Magnetic Structure of the Quasi-Two-Dimensional Antiferromagnet NpP₃. *Physical Review B* **2015**, *92*.
- (34) Lançon, D.; Walker, H. C.; Ressouche, E.; Ouladdiaf, B.; Rule, K. C.; McIntyre, G. J.; Hicks, T. J.; Rønnow, H. M.; Wildes, A. R. Magnetic Structure and Magnon Dynamics of the Quasi-Two-Dimensional Antiferromagnet FeP₃. *Physical Review B* **2016**, *94*.
- (35) Kim, T. Y.; Park, C. H. Magnetic Anisotropy and Magnetic Ordering of Transition-Metal Phosphorus Trisulfides. *Nano Lett* **2021**, *21*, 10114-10121.
- (36) Li, X.; Cao, T.; Niu, Q.; Shi, J.; Feng, J. Coupling the Valley Degree of Freedom to Antiferromagnetic Order. *Proceedings of the National Academy of Sciences of the United States of America* **2013**, *110*, 3738-3742.
- (37) Ni, Z.; Haglund, A. V.; Wang, H.; Xu, B.; Bernhard, C.; Mandrus, D. G.; Qian, X.; Mele, E. J.; Kane, C. L.; Wu, L. Imaging the Neel Vector Switching in the Monolayer Antiferromagnet MnP₃ with Strain-Controlled Ising Order. *Nature nanotechnology* **2021**, *16*, 782-787.

- (38) Ibañez-Azpiroz, J.; Tsirkin, S. S.; Souza, I. Ab Initio Calculation of the Shift Photocurrent by Wannier Interpolation. *Physical Review B* **2018**, *97*, 245143.
- (39) Xu, H.; Wang, H.; Li, J. Nonlinear Nonreciprocal Photocurrents under Phonon Dressing. *Physical Review B* **2022**, *106*.
- (40) Dai, Z.; Schankler, A. M.; Gao, L.; Tan, L. Z.; Rappe, A. M. Phonon-Assisted Ballistic Current from First-Principles Calculations. *Phys Rev Lett* **2021**, *126*, 177403.
- (41) Fei, R.; Song, W.; Pusey-Nazzaro, L.; Yang, L. Pt-Symmetry-Enabled Spin Circular Photogalvanic Effect in Antiferromagnetic Insulators. *Physical Review Letters* **2021**, *127*.
- (42) Xiao, R.-C.; Shao, D.-F.; Li, Y.-H.; Jiang, H. Spin Photogalvanic Effect in Two-Dimensional Collinear Antiferromagnets. *npj Quantum Materials* **2021**, *6*.
- (43) Kresse, G.; Joubert, D. From Ultrasoft Pseudopotentials to the Projector Augmented-Wave Method. *Physical Review B* **1999**, *59*.
- (44) Perdew, J. P.; Burke, K.; Ernzerhof, M. Generalized Gradient Approximation Made Simple. *Phys. Rev. Lett.* **1996**, *77*, 3865.
- (45) Monkhorst, H. J.; Pack, J. D. Special Points for Brillouin-Zone Integrations. *Phys. Rev. B* **1976**, *13*, 5188-5192.
- (46) Mostofi, A. A.; Yates, J. R.; Pizzi, G.; Lee, Y.-S.; Souza, I.; Vanderbilt, D.; Marzari, N. An Updated Version of Wannier90: A Tool for Obtaining Maximally-Localised Wannier Functions. *Computer Physics Communications* **2014**, *185*, 2309-2310.
- (47) Pizzi, G.; Vitale, V.; Arita, R.; Blugel, S.; Freimuth, F.; Geranton, G.; Gibertini, M.; Gresch, D.; Johnson, C.; Koretsune, T., et al. Wannier90 as a Community Code: New Features and Applications. *Journal of physics. Condensed matter : an Institute of Physics journal* **2020**, *32*, 165902.